Ultrawideband Tomographic Imaging in Uncalibrated Networks

Brian Beck, *Student Member, IEEE*, Xiaoli Ma, *Fellow, IEEE*, and Robert Baxley, *Senior Member, IEEE*

Abstract—This paper considers the problem of tomographic area mapping using radio frequency measurements gathered by a network of mobile nodes. Termed radio tomographic imaging, the technique has shown potential for object tracking, imaging static obstacles, and even through-wall imaging. Our approach addresses substantial issues for the practical implementation of such a system, namely, the mitigation of multipath signal effects and the characterization of a large number of uncalibrated network links. We propose a system that utilizes ultrawideband direct path signal strength measurements as a means of reducing the effects of the multipath fading. Furthermore, we address the estimation of unknown path loss and link bias parameters online through the framework of a linear mixed effects model. This permits the estimation of a static area map without a prohibitive calibration of these parameters prior to deployment, which is crucial in a network that may contain hundreds of links. Our model is posed as a convex optimization problem using the elastic net for regularization. Bayesian performance bounds are derived and our method shows positive results in simulation. We then demonstrate the efficacy of our solution on real tomographic data gathered from our cognitive spectrum operations testbed.

Index Terms—Calibration, radio tomographic imaging (RTI), ultra-wideband (UWB), wireless sensor networks.

I. INTRODUCTION

A. Background

THE use of wireless sensor networks has proliferated in the past decade, creating a wide body of research with many potential use cases. A network of numerous low-cost nodes may be static or mobile, collecting and transmitting a large array of possible data to be processed centrally, or in a distributed fashion. A key goal, particularly for mobile networks, is for the entire system to be *spatially* aware of its surroundings beyond the traditional localization of node positions. A networked robotic system may need to learn the locations of obstacles to be avoided, as in a simultaneous localization and mapping (SLAM) algorithm [1], [2]. Environmental monitoring applications may additionally require the network to know the presence of people entering or leaving an area, even tracking their movements [3]. Networks employing radio frequency (RF) communication may need to estimate channel quality between points in space, as in [4]. Finally, a mobile network may benefit from environmental map information in areas which are visually occluded behind walls or other obstructions. Such through-wall images could be used by emergency personnel or soldiers in a combat situation [5].

Tomographic imaging is a promising means for achieving the aforementioned goals. Most generally, tomography is the process of reconstructing an image of some environment by viewing it through slices or sections. In practice, this usually means sending some type of energy-carrying signal through an object or area, and observing attenuation in the signal at another position. Over many spatially diverse measurements, an appropriate inverse model may be applied to estimate the environment. Use of RF waves as the measurement phenomenon is attractive due to their potential to propagate over wide areas and penetrate a variety of materials. Early efforts in RF tomographic techniques attempted to locate discontinuities in the ground, such as coal seams or tunnels [6]–[9].

In the past decade, the proliferation of low cost wireless sensor networks has stimulated additional research interest in tomographic area mapping and tracking. The term RTI has been used to describe the use of RF signals to estimate the shadowing loss due to static or moving objects [10]. RTI is posed as a case of device-free localization, as the objects to be located do not carry transmitters or receivers [11]. In [10], the authors proposed to image changes in RF attenuation from a measured baseline using only received signal strength (RSS), a measurement available to almost any radio receiver. In [12], measurements of RSS variance were used for tracking only the moving objects in an environment, emphasizing the through-wall capabilities of RTI. Methods for addressing regularization of the inverse problem of image reconstruction were explored in [13].

Other authors have pursued the tomographic imaging of the purely static features of an environment. Knowledge of the static shadowing environment is useful for mapping obstacles, estimating link shadow fading [14], and even informing localization algorithms [15]. In [16], the author utilized a pair of robots moving in coordinated patterns to collect RSS data for a variety of attenuating structures. Compressive sampling techniques were used to reconstruct images using a reduced number of measurements. Reference [17] explored

the relationship between random and coordinated spatial sampling patterns using the same robotic testbed. In [18], the authors demonstrated the benefits of sensor fusion for observable and unobservable features, combining laser and RF measurements.

While the aforementioned works have focused on narrowband RF imaging, UWB pulse radio techniques have also attracted interest. A UWB radio signal is often defined as having a bandwidth greater than 20% of the center frequency, or 500 MHz, whichever is greater. We also distinguish a UWB signal from other wideband signals, such as spread spectrum, by the impulse nature of UWB. That is, UWB signals achieve high bandwidth via very short duration pulses of very low duty cycle. The resulting short spatial extent of the waveforms results in several advantages, namely high range resolution, interference resistance, and multipath signal rejection [19].

These advantages have led to applications in traditional radar tracking, through-wall imaging, and localization. In fact, radar based approaches dominate the UWB literature for imaging objects occluded by walls, e.g. [20]–[23]. For indoor object detection and tracking, a holistic design of the UWB sensor network is considered in [24], and selection of representative measurements is addressed in [25]. UWB signals have even been employed for the remote monitoring of human breathing [26]. In addition to imaging and tracking, UWB has shown promise for the precise localization of nodes in sensor networks where GPS is unavailable. Accurate time-of-arrival (TOA) information, and even two-way time-of-flight (TOF) measurements made by UWB radios can resolve the distances between cooperative nodes, to which a localization algorithm may be applied [27]–[30].

B. Contributions

In this paper, we address the RTI problem for imaging the static features and obstacles in the environment using UWB signaling techniques in a realistically deployable mobile network. Our approach has several advantages, and seeks to address some problems with practical implementation of RTI systems. The first problem is mitigation of multipath signal effects which are detrimental to tomographic models which consider only the line-of-sight (LOS) signal path. As the authors of [31] showed, small scale multipath effects can easily exceed the shadowing effects we are interested in, showing up as additional noise in the measurements. We address this issue by using the large signal bandwidth of UWB to clearly separate the LOS signal path from the reflected multipath signal energy, by using a direct-path signal strength (DPSS) metric. Doing so is highly beneficial for applying a linear tomographic projection model along the LOS, and employing a straightforward path loss model even in multipath rich indoor environments. The authors of [16]–[18] mitigated these multipath effects using high gain directional antennas, which were kept oriented toward each other at all times. Our approach can be performed with basic, omni-directional broadband antennas, thus achieving the multipath separation capability regardless of the loca-

tions or antenna orientations of the nodes. This is important for scaling the network beyond a single pair of nodes, where reorienting antennas across the many links would become intractable.

Second, we address the calibration issue which is present in static object imaging for RTI. When imaging static objects, the shadowing losses of interest must be separated from the path losses due to link distance, the multipath signal effects, as well as the systematic effect of each link. Differences in transmit power, cable lengths, antenna gain, receiver sensitivity, etc. all introduce an unknown bias for *each* link in the network. Some authors, e.g. [32], [33] have addressed this problem for tracking moving objects, where only changes in RSS are measured. Others [10], [34] collect baseline data for static nodes in an "empty" area, then insert the shadowing objects to be measured. Still others [16]–[18] have only a single mobile link to characterize. However, as the network scales beyond even a couple of nodes, individual characterization of each link prior to deployment may be infeasible. During deployment, a given mobile link may not know if or when it is being shadowed by objects, making simple online calibration difficult. We propose to jointly estimate both the unknown spatial shadowing due to objects, as well as the unknown link bias and system path loss parameters. We do this under the framework of a linear mixed effects model. The problem is convex, which leads to efficient numerical solution methods. To overcome the underdetermined nature of the tomography problem, we implement a regularization technique known as the elastic net (EN). This allows the inclusion of the a-priori constraints of image pixel sparsity, as well as assumed pixel spatial correlation.

The paper is organized into sections as follows. Section II describes our use of the UWB signal to isolate direct path signal energy for measurements, as well as modeling the signal propagation. In Section III we describe the tomographic projection model used to map an image on to the space of measured data. Our mixed-effects image reconstruction model is detailed in Section IV. We derive performance bounds for the model and test its performance in Sections V and VI, respectively. The results of our tomographic experiments are displayed in Section VII. Finally, we conclude and discuss future work in Section VIII.

II. UWB Sampling, Measurement, and Propagation

A. Time Domain Direct Sampling

Since a UWB signal pulse is very short in both temporal and spatial extent, it will therefore occupy a large bandwidth in the frequency domain. However, the total transmitted signal power may be quite small (< -14.8 dBm in our testing). This is generally to comply with regulations governing UWB transmissions; for example the Federal Communications Commission (FCC) requires the power spectrum to be below -41.3 dBm/MHz. This low limit gives a UWB transmission near noise-level characteristics when viewed from the frequency domain, quite unlike narrowband communication signals. As a result, UWB signals are generally analyzed directly from samples in the time domain. This of course
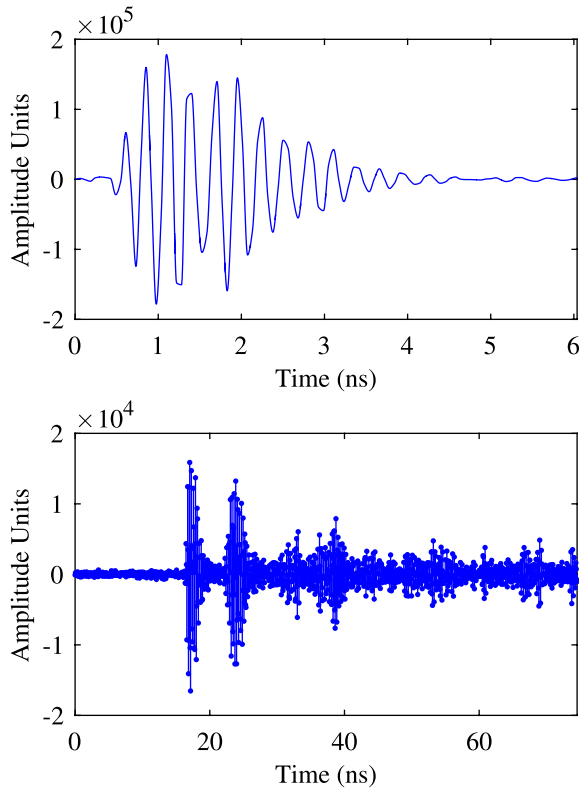
Fig. 1. Top: Idealized transmitted UWB pulse signal. Bottom: Actual time domain received samples in a high multipath indoor environment at a distance of 10 meters. Amplitude is the raw ADC/DAC value, assumed proportional to voltage.

requires relatively high sampling rates in order to satisfy the Nyquist criterion. For example, the P410 UWB radio from Time Domain[1] used in our experiments has an effective sampling period of 61 ps.

Fig. 1 shows an example idealized pulse transmitted from the UWB radio. The pulse is designed as a bandpass signal with center frequency 4.3 GHz and bandwidth 2.2 GHz, with power level conforming to FCC requirements. The transmitted signal is sampled by another UWB transceiver and the received pulse is shown in the bottom plot of Fig. 1. Both transmitter and receiver are operating in a high multipath indoor environment. The many surfaces in a multipath environment produce signal reflections that arrive at the receiver at different times. In fact, a majority of the received signal's energy is due to multipath propagation. However, the shortest path along the LOS between transmitter and receiver arrives first, and is clearly separated from the reflected energy by direct sampling in the time domain. This is the motivation for our definition and use of direct-path signal strength, described below.

B. Direct-Path Signal Strength

The ability to separate the LOS and multipath signal energy is crucial, since a linear tomographic projection only models shadowing loss along the LOS. If not rejected, the multipath energy creates a rapidly fading channel, and the RSS variance

[1]Time Domain Corporation, Huntsville, AL. Available at: http://www.timedomain.com.

can become extremely large, as noted in [31]. The result is unacceptably noisy measurements for tomographically estimating the large-scale shadowing loss due to objects along the LOS. To measure the LOS-only signal strength, we make use of the DPSS metric. Originally defined in [35], the DPSS was empirically determined to provide the best measure of signal strength along the LOS path. The metric is defined by

$$Y = \max_{\forall l} |x[l]w[l-\tau]|, \qquad (1)$$

where $x[l]$ is the sampled signal and $w[l-\tau]$ is a unit amplitude rectangular window of the same duration as the transmitted pulse. The offset τ is the sample index of the detected leading edge of the signal. In practice, to reduce the variance of the DPSS and improve SNR, multiple pulses are accumulated and averaged to obtain a single measurement, which we will still denote simply as Y. This is the measure of signal strength used throughout the paper. Note that while the RTI literature generally uses power as the signal strength metric, Y is a measure of amplitude, being an average of many pulse peaks as measured by the ADC in Fig. 1. Rather than square this value to obtain units of power, we will simply express Y in the dB scale in the next section.

C. Log-Distance Path Loss Model

The UWB multipath propagation channel has been studied in theory and empirically, e.g. [36], [37]. In this paper, we express the DPSS as a function of distance and shadowing using a simplified log-distance path loss model. The model is expressed with additive terms in the log domain as

$$y = b + s - \alpha d + \epsilon, \qquad (2)$$

where DPSS value $y = 20 \log_{10} Y$ is now measured in dB. $b \in \mathbb{R}$ is a bias or "gain" term aggregating the effects of transmitter power, receiver sensitivity, antenna gains, cable losses, etc. $s \in (-\infty, 0]$ is the shadowing component of primary interest in this work; s models the signal strength loss in the observed variable y due to objects blocking the LOS. $\alpha > 0$ is a path loss exponent controlling the rate of signal decay due to distance, with d equal to the log-distance between transmitter and receiver. The additive error term $\epsilon \in \mathbb{R}$ represents measurement error and any other unmodeled effects.

To characterize b and α in (2) for a single transmitter/receiver pair, we have performed a LOS path loss experiment in a multipath rich laboratory environment over the distances of interest. The results are plotted in Fig. 2. The results show a strong fit to the measured data, indicating that (2) is a reasonable model for DPSS path loss in indoor environments. The large dB values shown in Fig. 2 are relative to 1 amplitude unit, since proportionality constants for units of energy/voltage are not known. For example, the P410 ADC outputs DPSS values in the typical range of 5000 to 60000 amplitude units.

In order to produce a tomographic image of the shadowing caused by objects in the environment, many DPSS measurements must be taken at spatially diverse locations in that environment. This is facilitated by mobile sensor networks which may contain many links; M mobile nodes grants up
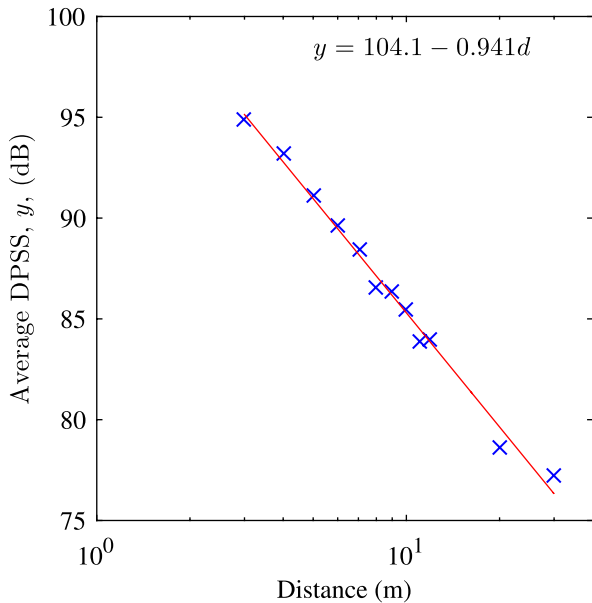
Fig. 2. Measured DPSS for a single LOS ($s = 0$) link in an indoor environment. The least squares values for the path loss parameters are $\hat{b} = 104.1$, $\hat{a} = 0.941$, with $r^2 = 0.99$. 1000 DPSS measurements were averaged for each data point.

Fig. 3. Graphical depiction of relative pixel weighting and indexing for an arbitrary link i taking a measurement j in a 10×10 pixel image. Shaded pixels have $x_{ijk} > 0$ according to (6); unshaded pixels have $x_{ijk} = 0$. Note the single index k is used to designate the K pixels by column stacking, typical in image processing contexts.

to $N = M^2 - M$ unique transmit/receive pairs. We index (2) to encompass the full network by using i to index the unique links, and j to index the individual measurements made by a given link:

$$y_{ij} = b_i + s_{ij} - \alpha d_{ij} + \epsilon_{ij}. \tag{3}$$

Thus, y_{ij} is the jth DPSS measurement made by the ith link in the network. The index set is defined by $i \in \{1...N\}$, where $N = M^2 - M$. The links are formed by the M nodes in the network, and each link makes n_i measurements. The gain term is now also indexed by i, since transmit power, receiver sensitivity, and other systematic effects mentioned above are different for each transmit/receive pair, and may vary substantially. The LOS shadowing s_{ij} and link log-distance d_{ij} may change with each measurement as the nodes move, and are indexed accordingly. The unknown path loss exponent α is assumed to be an environmental variable shared by all links and thus carries no index. Note that for a spherical wave propagating in free space $\alpha = 1$ for signal strength measurements, though in practice will vary due to antenna properties and the environment.

Clearly, the link index i creates a large number of bias parameters $\{b_i, \alpha\}$. Thus, single-link characterizations such as those shown in Fig. 2 may not generalize well across the entire network, leading to poor or misleading results, even with homogeneous hardware. Our mixed effects estimation procedure, derived in the following sections, seeks to characterize these parameters, along with the unknown spatial shadowing.

III. TOMOGRAPHIC PROJECTION MODEL

From the path loss model in (3), the DPSS measurements y_{ij} contain information about the shadowing loss along the LOS for that measurement. This information, when aggregated, should describe the static shadowing losses in the
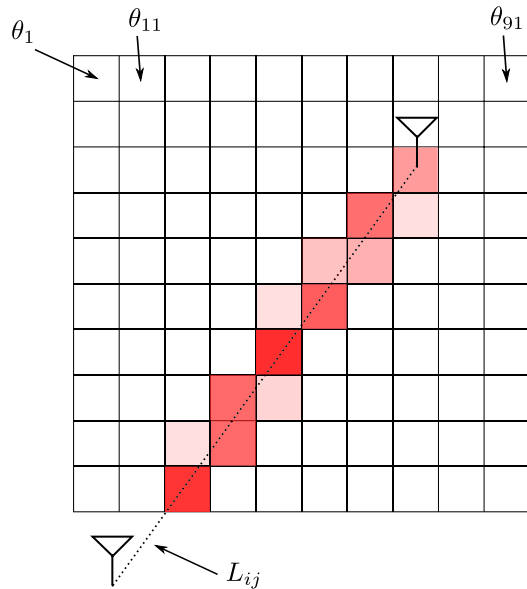
environment as a function of space. This rate of attenuation with respect to spatial extent has been termed the spatial loss field (SLF) [14], [38], and its estimation is our primary goal. Allowing the spatial variable $\mathbf{z}$ to represent position, the total shadowing loss s_{ij} between two points is described as the line integral of the continuous SLF $\theta(\mathbf{z})$ over the straight line connecting the two points,

$$s_{ij}\big(\theta(\mathbf{z}), L_{ij}\big) = \int_{L_{ij}} \theta(\mathbf{z})\, d\mathbf{z}, \tag{4}$$

where L_{ij} is the straight line path connecting the transmitter and receiver of link i when taking measurement j. From (4) it can be seen that the SLF has units of dB per meter if measuring distance in meters. Also, given the sign conventions used in Section II-C, $\theta(\mathbf{z}) \in (-\infty, 0]$ will be negative in regions containing attenuating objects, and zero in free space regions.

In seeking a tractable method of estimating the entire SLF from measurements, we approximate the integral with a summation, and replace the continuous SLF $\theta(\mathbf{z})$ with a vector $\boldsymbol{\theta}$ having a discrete set of K pixel values. This yields

$$s_{ij} = \sum_{k=1}^{K} x_{ijk}\theta_k = \mathbf{x}_{ij}^T \boldsymbol{\theta}. \tag{5}$$

Now, the shadowing loss is the sum over all SLF pixels θ_k in the area to be imaged, multiplied by a corresponding set of pixel weights x_{ijk}. These weights represent each pixel's contribution to the total shadowing loss. Note that though the SLF is interpreted as a two-dimensional map, in (5) the SLF is expressed as a $K \times 1$ vector by column stacking, consistent with the image processing literature.

In assigning weights x_{ijk}, we choose the straight line approach, depicted in Fig. 3. In this weighting only pixels along the direct LOS between transmitter and receiver receive

nonzero weight. This is due to the fact that the DPSS measurement effectively eliminates the multipath signal components, such that only objects within pixels along the LOS should materially affect the shadowing loss. The notation $\theta_k \in L_{ij}$ will indicate that the straight line segment from transmitter to receiver passes through pixel θ_k. The weighting values are then assigned by

$$x_{ijk} = \begin{cases} D_k : & \theta_k \in L_{ij} \\ 0 : & \text{else,} \end{cases} \quad (6)$$

where D_k is the length of the line segment passing through pixel θ_k. This weighting scheme is similar to those used in X-ray based computed tomography (CT) scanning, as also noted in [34]. Weighting each pixel by line segment length also preserves the expected units of measurement for the model; x_{ijk} has units of meters, θ_k has units of dB per meter, yielding the shadowing loss in pure dB of attenuation.

The aforementioned straight line weight model makes physical sense for the DPSS metric, since the LOS path is isolated. However different propagation models have also been considered in the RTI literature. In [10] and [12], an evenly weighted ellipse with transmitter and receiver as foci was used. The weight factor was inversely proportional to the square root of the link distance, which represents the lower RSS variance for longer links. In [34], several models were studied from experimental data, including both elliptical and straight line weighting areas.

We also expect that shadowing losses will be spatially correlated in practice. Therefore we will define the between-pixel spatial covariance matrix

$$E\left[\boldsymbol{\theta}\boldsymbol{\theta}^T\right] - E[\boldsymbol{\theta}] E[\boldsymbol{\theta}]^T = \mathbf{C}_{\boldsymbol{\theta}} \in \mathbb{R}^{K \times K}. \quad (7)$$

To determine the elements of $\mathbf{C}_{\boldsymbol{\theta}}$, we assume that the between-pixel covariance decays exponentially with distance,

$$E\left[\theta_k \theta_l\right] - E\left[\theta_k\right] E\left[\theta_l\right] = \sigma_\theta^2 e^{-\frac{D_{kl}}{\kappa}}, \quad (8)$$

where D_{kl} is the distance between the centers of pixels θ_k and θ_l, and κ is a spread parameter with units of meters. This exponential decay parametrization is similar to that used in the network shadowing model of [14] to model randomly placed objects, and was used in the experimental work of [34] as *a-priori* image information. We use the empirically determined value of $\kappa = 0.21$ m from [14] in our work. We also set the prior pixel variance $\sigma_\theta^2 = 1$, as the overall scaling effect will be managed by selection of regularization parameter λ_2 in Section IV-B.

Note that other characterizations of pixel correlation besides that in (8) are possible. In our work in [39] for example, we explored using *a-priori* knowledge of image structure expressed as covariance to enhance image reconstruction. However, we have not done so in this work in order to minimize assumptions.

IV. MIXED EFFECTS IMAGE RECONSTRUCTION

This section describes our full forward model mapping the unknown SLF onto the known DPSS measurements.

The inverse problem of retrieving an estimate of the SLF image is ill-conditioned, and thus requires regularization to obtain a useful result. We explain our approach to regularization using a modified form of the EN cost function, and its solution using convex optimization.

A. Forward Model

By combining (3) and (5), we obtain an expression for the K unknown SLF parameters as a function of the observed DPSS measurements:

$$y_{ij} = \mathbf{x}_{ij}^T \boldsymbol{\theta} + b_i - \alpha d_{ij} + \epsilon_{ij}. \quad (9)$$

As given in Section II, each link in the network makes n_i measurements. To simplify the notation we will assume that each link makes the same number of measurements, so that $n_i = n.$[2] Aggregating the n measurements made by link i yields the expression

$$\begin{aligned}
\mathbf{y}_i &= \begin{bmatrix} \mathbf{x}_{i1}^T \\ \vdots \\ \mathbf{x}_{in}^T \end{bmatrix} \boldsymbol{\theta} + b_i \begin{bmatrix} 1 \\ \vdots \\ 1 \end{bmatrix} + \alpha \begin{bmatrix} -d_{i1} \\ \vdots \\ -d_{in} \end{bmatrix} + \begin{bmatrix} \epsilon_{i1} \\ \vdots \\ \epsilon_{in} \end{bmatrix} \\
&= \mathbf{X}_i \boldsymbol{\theta} + b_i \mathbf{1}_n + \alpha \mathbf{d}_i + \boldsymbol{\epsilon}_i \\
&= \begin{bmatrix} -\mathbf{d}_i & \mathbf{X}_i \end{bmatrix} \begin{bmatrix} \alpha \\ \boldsymbol{\theta} \end{bmatrix} + b_i \mathbf{1}_n + \boldsymbol{\epsilon}_i \\
&= \mathbf{H}_i \boldsymbol{\theta}^{(\alpha)} + b_i \mathbf{1}_n + \boldsymbol{\epsilon}_i. \quad (10)
\end{aligned}$$

Here we have defined the design matrix $\mathbf{X}_i \in \mathbb{R}^{n \times K}$ as the stacked, transposed pixel weight vectors defined for each individual measurement in (5). Defining $\mathbf{1}_n$ to be an $n \times 1$ vector of ones, the vector $b_i \mathbf{1}_n$ replicates the nuisance parameter representing the bias of link i for each measurement. The vector $\alpha \mathbf{d}_i \in \mathbb{R}^n$ maps the contribution of the unknown path loss exponent onto the DPSS measurements via the known log distances. Finally, the collected errors form the vector $\boldsymbol{\epsilon}_i \in \mathbb{R}^n$. For compactness, we combine the unknowns not dependent on link index i into a single vector $\boldsymbol{\theta}^{(\alpha)} \in \mathbb{R}^{K+1}$ with corresponding known model matrix $\mathbf{H}_i \in \mathbb{R}^{n \times (K+1)}$.

From (10), we can see that the measurements for each link $\mathbf{y}_i$ are a function of the common SLF/path loss exponent parameter $\boldsymbol{\theta}^{(\alpha)}$, which is of primary interest and does not vary with each link i. However, DPSS is also a linear function of the link biases $\{b_i\}$, which are unique to each link and unknown. From here on we will model b_i as a Gaussian random variable with unknown mean and variance; so that $b_i \sim \mathcal{N}(\mu_b, \sigma_b^2)$. The $\boldsymbol{\epsilon}_i$ is modeled as a zero-mean independent Gaussian random vector; $\boldsymbol{\epsilon}_i \sim \mathcal{N}(\mathbf{0}, \sigma_\epsilon^2 \mathbf{I}_n)$. Thus within link i, we explicitly separate the link bias b_i from independent noise vector $\boldsymbol{\epsilon}_i$. We also assume that the $\{b_i, \boldsymbol{\epsilon}_i\}$ are mutually independent, and independent across i.

Under these assumptions, (10) has the general form of a linear *mixed effects model*, a special class of linear models used in the statistical literature. Such models are used to express the hierarchical effects of clustered data which might be arranged into "bins". That is, they account for measurement effects at different levels: global effects which are of primary interest, and subject or group specific effects which are not of primary

---

[2]It is straightforward to generalize these results such that each link makes a variable number of measurements.

interest but nevertheless must be accounted for [40] and [41]. Thus, they are a natural fit for modeling the unknown bias and path loss present in a network making signal strength measurements. The term *mixed effects* is used because we model the global parameters $\boldsymbol{\theta}^{(\alpha)}$ as fixed but unknown "fixed effects", while the link specific effects $\{b_i, \boldsymbol{\epsilon}_i\}$ are modeled as random variables, or "random effects" (REs). While we will not specifically use the Gaussian assumption of the $\{b_i\}$ for image reconstruction, doing so facilitates closed form derivation of the Cramér Rao lower bound (CRLB), and is in general agreement with our empirical results.

To obtain a single linear model from the N sets of equations, (10) is stacked for each value of i by

$$
\mathbf{y} = \begin{bmatrix} \mathbf{y}_1 \\ \vdots \\ \mathbf{y}_N \end{bmatrix} = \begin{bmatrix} \mathbf{H}_1 \\ \vdots \\ \mathbf{H}_N \end{bmatrix} \boldsymbol{\theta}^{(\alpha)}
$$

$$
+ \begin{bmatrix} \mathbf{1}_n & \mathbf{0} & \cdots & \mathbf{0} \\ \mathbf{0} & \mathbf{1}_n & & \vdots \\ \vdots & & \ddots & \mathbf{0} \\ \mathbf{0} & \cdots & \mathbf{0} & \mathbf{1}_n \end{bmatrix} \begin{bmatrix} b_1 \\ \vdots \\ b_N \end{bmatrix} + \begin{bmatrix} \boldsymbol{\epsilon}_1 \\ \vdots \\ \boldsymbol{\epsilon}_N \end{bmatrix}
$$

$$
= \mathbf{H}\boldsymbol{\theta}^{(\alpha)} + \mathbf{Z}\mathbf{b} + \boldsymbol{\epsilon}. \tag{11}
$$

Here the full data vector is $\mathbf{y} \in \mathbb{R}^{N_T}$, where $N_T = Nn$ is the full data size. The full model matrices have dimensions $\mathbf{H} \in \mathbb{R}^{N_T \times (K+1)}$ and $\mathbf{Z} \in \mathbb{R}^{N_T \times N}$. The unknown SLF vector $\boldsymbol{\theta}^{(\alpha)} \in \mathbb{R}^{(K+1)}$ is unchanged, and $\mathbf{b} \in \mathbb{R}^N$ is the full unknown mixed effects vector. The modeling errors/measurement noise is captured by vector $\boldsymbol{\epsilon} \in \mathbb{R}^{N_T}$. Thus (11) relates all parameters, known and unknown, to the collected data $\mathbf{y}$ across all links in the network, and serves as our full forward measurement model.

B. EN Regularization

Inverse problems in the literature on mixed effects are generally solved using a maximum likelihood approach in which the data covariance and unknown fixed effects are estimated simultaneously [40]. However, (11), like most imaging inverse problems, represents an underdetermined system of equations. That is, the measurement data are insufficient to fully describe the parameter $\boldsymbol{\theta}^{(\alpha)}$, yielding an infinite number of candidate solutions which fit the data $\mathbf{y}$. Model matrix $\mathbf{H}$ has low rank, which is due to a combination of limited measurements, each measurement describing only a small part of $\boldsymbol{\theta}^{(\alpha)}$, and disparities in areas of the image crossed by few or no links. A full rank model matrix $\mathbf{H}$ is normally assumed in the mixed effects literature; thus the usual parametric solution of mixed models, e.g., maximum likelihood, will not yield useful images.

As a result, prior information must be introduced into the model to select a unique solution among the infinite number available, a process known as regularization. This usually involves minimizing some cost function of the data and unknown parameters, selecting the "best" value for $\boldsymbol{\theta}^{(\alpha)}$ which minimizes the cost function. Regularization is thus

a nonparametric approach to solving (11). Several popular methods exist, such as Tikhonov (2-norm), lasso (1-norm), truncated singular value decomposition, and total variation approaches [42]. Each method has its own tradeoffs; in [10], Tikhonov regularization was preferred for computational speed and having a closed form solution. In [16]–[18], total variation minimization was preferred to enforce piecewise constant shadowing regions.

In our approach, we use the EN. Originally proposed in [43], the EN loss function is a linear combination of Tikhonov and lasso type penalties, given by

$$
L(\lambda_1, \lambda_2, \boldsymbol{\theta}) = \|\mathbf{y} - \mathbf{X}\boldsymbol{\theta}\|_2^2 + \lambda_2 \|\boldsymbol{\Gamma}\boldsymbol{\theta}\|_2^2 + \lambda_1 \|\boldsymbol{\theta}\|_1 \tag{12}
$$

for the basic linear model $\mathbf{y} = \mathbf{X}\boldsymbol{\theta} + \boldsymbol{\epsilon}$. The 2-norm penalty $\|\boldsymbol{\Gamma}\boldsymbol{\theta}\|_2^2$ is taken from Tikhonov regularization, also known as ridge regression, and penalizes the energy in $\boldsymbol{\Gamma}\boldsymbol{\theta}$, for some specified linear operator $\boldsymbol{\Gamma}$. The 1-norm penalty $\|\boldsymbol{\theta}\|_1$ comes from the lasso regression, and enforces a sparse solution. Parameters $\{\lambda_2, \lambda_1\} > 0$ control the penalty term's smoothing effect on the solution.

Several unique properties of the EN are noted in [43] which are appropriate for the assumptions in our problem. First, the 1-norm penalty enforces a sparse solution, with many elements of $\boldsymbol{\theta}$ forced to zero. This is appropriate as we assume that much of the area to be imaged consists of empty space, which has shadowing loss equal to zero. 2-norm-only regularization methods will in general have all $\theta_k \neq 0$. Second, the addition of the 2-norm penalty from Tikhonov regularization overcomes what is known as a grouping effect of the lasso. If a subset of parameters $\boldsymbol{\theta}_c \subset \boldsymbol{\theta}$ are highly correlated, then the lasso will tend to select only one of them at random. This grouping effect is undesirable for our model; in Section III we assume shadowing losses to be correlated among neighboring pixels in the image.

To model this expected behavior, we define the *a-priori* pixel covariance according to (7) and (8). Use of a prior covariance matrix is of course probabilistic and suggests a Bayesian interpretation of the data. However, (12) is a deterministic cost function of the unknowns. It has been observed, e.g., [44], that the 2-norm Tikhonov penalty can be related to the Bayesian covariance via

$$
\|\boldsymbol{\Gamma}\boldsymbol{\theta}\|_2^2 = \boldsymbol{\theta}^T \boldsymbol{\Gamma}^T \boldsymbol{\Gamma} \boldsymbol{\theta} = \boldsymbol{\theta}^T \mathbf{C}_{\boldsymbol{\theta}}^{-1} \boldsymbol{\theta}, \tag{13}
$$

so that $\boldsymbol{\Gamma}$ can be derived from $\mathbf{C}_{\boldsymbol{\theta}}^{-1}$ via the Cholesky decomposition. In this way the assumed pixel covariance may be incorporated into the 2-norm regularization term in (12).

Finally, we extend the EN cost function of (12) by incorporating our additional mixed effects model terms:

$$
\widetilde{L}(\lambda_1, \lambda_2, \boldsymbol{\theta}, \alpha, \mathbf{b})
$$
$$
= \left\| \mathbf{y} - \mathbf{H}\boldsymbol{\theta}^{(\alpha)} - \mathbf{Z}\mathbf{b} \right\|_2^2 + \lambda_2 \|\boldsymbol{\Gamma}\boldsymbol{\theta}\|_2^2 + \lambda_1 \|\boldsymbol{\theta}\|_1. \tag{14}
$$

Here the squared-error term seeks to obtain agreement between the solution and the data, where we now allow the individual link bias terms $\mathbf{b}$ to be model variables to be estimated. The linear operator $\boldsymbol{\Gamma}$ allows us to enforce the per-pixel spatial correlations desired above. Note that the penalty terms apply to vector $\boldsymbol{\theta}$ only, that is, regularization is not applied to variable α.

Given the regularization parameters, the minimization problem with all constraints is

$$\left\{ \hat{\boldsymbol{\theta}}, \hat{a}, \hat{\mathbf{b}} \right\} = \underset{\boldsymbol{\theta} \leq 0, a > 0}{\arg \min} \; \widetilde{L}\left(\boldsymbol{\theta}, \alpha, \mathbf{b} \,|\, \lambda_1, \lambda_2\right). \quad (15)$$

The constraint $\boldsymbol{\theta} \leq 0$ indicates that all elements of the solution vector are less than or equal to zero, consistent with the definition. While there is no known closed-form solution to the EN, both it and our extension in (14) represent convex cost functions. Thus, efficient methods exist for finding numerical solutions, and flexible software packages are available. For our simulation and experimental results, we have employed the CVX package for MATLAB, which allows specifying and solving various convex problems [45].

This leaves the problem of determining the parameters $\{\lambda_2, \lambda_1\}$ which adjust the regularization weighting to apply. Higher values will generally result in smoother images, with fewer pixels selected as nonzero. While multiple methods exist to determine regularization parameters, we use the two step method suggested in [43]. In the first step, the usual Tikhonov regularization is performed, that is, with $\lambda_1 = 0$ for a range of values of λ_2. For each λ_2, we plot the observed "norm error" $\|\boldsymbol{\Gamma}\hat{\boldsymbol{\theta}}(\lambda_2)\|_2^2$ as a function of the corresponding "data error" $\|\mathbf{y} - \mathbf{H}\hat{\boldsymbol{\theta}}^{(a)}(\lambda_2) - \mathbf{Z}\hat{\mathbf{b}}(\lambda_2)\|_2^2$. For a wide range of λ_2 values, this curve will take an "L" shape, and hence this procedure is referred to as the L-curve method. The λ_2 value corresponding to the inflection point at which the sum of the two error terms is minimized is the value used. This heuristic is justified by its general robustness and intuition as a compromise between the two solution norms.

For λ_1, leave-one-out cross validation is used. A single data point is omitted from each link's measurements, forming a "training" data set and associated model matrices $\{\mathbf{y}_t, \mathbf{H}_t, \mathbf{Z}_t\}$. The left out data forms a smaller "verification" data and model matrix set, $\{\mathbf{y}_v, \mathbf{H}_v, \mathbf{Z}_v\}$. A suitable range of values for λ_1 are chosen to test, denoted $\{\lambda_{1,q}\}, \; q = 1...Q$. Then a solution pair $\hat{\boldsymbol{\theta}}_q^{(a)}, \hat{\mathbf{b}}_q$ is computed for each $\lambda_{1,q}$ using the training set. For each candidate solution, we calculate the prediction error $\|\mathbf{y}_v - \mathbf{H}_v\hat{\boldsymbol{\theta}}_q^{(a)} - \mathbf{Z}_v\hat{\mathbf{b}}_q\|_2^2$ using the verification set. Finally, we choose the $\lambda_{1,q}$ corresponding to the $\hat{\boldsymbol{\theta}}_q, \hat{\mathbf{b}}_q$ that gave the lowest prediction error. With both $\{\lambda_1, \lambda_2\}$ now selected, a full solution can be computed using the entire data set via (15).

V. BAYESIAN CRLB DERIVATION

It is very useful to obtain performance bounds for a given model and solution method to benchmark performance in the general case. The CRLB is very well known in statistics as a lower bound on the variance of unbiased estimators. The CRLB proves that the variance of individual parameter estimates are lower bounded by corresponding elements of the inverse Fisher information matrix. However, our estimator in (15) is clearly biased by the introduction of the regularization terms. In such cases the CRLB has been extended to include biased estimators in what is known as the Bayesian CRLB, or Van Trees inequality [46]. The covariance of biased estimators is bounded by the inclusion of a prior distribution on the unknowns, just as

in Bayesian estimation. This leads to the derivation of a Fisher information matrix for both the data likelihood and the prior. The Bayesian CRLB states that the estimation error covariance matrix $\mathbf{E} = E[(\hat{\boldsymbol{\theta}}^{(a)} - \boldsymbol{\theta}^{(a)})(\hat{\boldsymbol{\theta}}^{(a)} - \boldsymbol{\theta}^{(a)})^T]$ is lower bounded by

$$\mathbf{E} \succeq (\mathbf{F}_L + \mathbf{F}_P)^{-1} = \mathbf{F}^{-1}, \quad (16)$$

where $\mathbf{F}_L, \mathbf{F}_P$ are the Fisher information matrices for the data log likelihood and prior distributions, respectively. The "$\succeq$" relation indicates that the difference matrix $\mathbf{E} - \mathbf{F}^{-1}$ is positive semidefinite. An important consequence of this fact is that the diagonal elements of $\mathbf{E}$ represent lower bounds on the variance of estimating individual pixel values; that is,

$$\mathbf{E}_{qq} = E[(\hat{\boldsymbol{\theta}}^{(a)} - \boldsymbol{\theta}^{(a)})_q^2] \succeq \mathbf{F}_{qq}^{-1}. \quad (17)$$

Though other formulae exist, the Fisher information expressions for general data log likelihood and prior distributions can be expressed as

$$\mathbf{F}_L = E_{\mathbf{y}|\boldsymbol{\theta}} \left[(\nabla_{\boldsymbol{\theta}} \mathscr{L}(\mathbf{y}|\boldsymbol{\theta})) (\nabla_{\boldsymbol{\theta}} \mathscr{L}(\mathbf{y}|\boldsymbol{\theta}))^T \right] \quad (18)$$

$$\mathbf{F}_P = E_{\boldsymbol{\theta}} \left[(\nabla_{\boldsymbol{\theta}} \mathscr{L}(\boldsymbol{\theta})) (\nabla_{\boldsymbol{\theta}} \mathscr{L}(\boldsymbol{\theta}))^T \right], \quad (19)$$

where $\mathscr{L}(\cdot)$ indicates the log PDF of the enclosed random vector. ∇ represents the gradient operator taken with respect to the unknown parameter as shown. We will now derive the necessary expressions to compute a Bayesian CRLB for our mixed effects model in (10), and use it to benchmark simulated performance. From (10), the data have Gaussian distribution $\mathbf{y}_i \sim \mathcal{N}(\boldsymbol{\mu}_{\mathbf{y}_i}, \mathbf{C}_{\mathbf{y}_i})$, where

$$\boldsymbol{\mu}_{\mathbf{y}_i} = \mathbf{H}_i \boldsymbol{\theta}^{(a)} + \mu_b \mathbf{1}_n \quad (20)$$

$$\mathbf{C}_{\mathbf{y}_i} = \sigma_b^2 \mathbf{1}_n \mathbf{1}_n^T + \sigma_\epsilon^2 \mathbf{I}_n. \quad (21)$$

The data log likelihood is then given by (up to constant terms not dependent on $\boldsymbol{\theta}^{(a)}$):

$$\mathscr{L}\left(\mathbf{y}_i | \boldsymbol{\theta}^{(a)}\right) = -\frac{1}{2} \left(\mathbf{y}_i - \boldsymbol{\mu}_{\mathbf{y}_i}\right)^T \mathbf{C}_{\mathbf{y}_i}^{-1} \left(\mathbf{y}_i - \boldsymbol{\mu}_{\mathbf{y}_i}\right). \quad (22)$$

Using straightforward rules for the gradient operator over vectors, it can be easily shown that

$$\nabla_{\boldsymbol{\theta}^{(a)}} \mathscr{L}\left(\mathbf{y}_i | \boldsymbol{\theta}^{(a)}\right) = \mathbf{H}_i^T \mathbf{C}_{\mathbf{y}_i}^{-1} \left(\mathbf{y}_i - \boldsymbol{\mu}_{\mathbf{y}_i}\right) = \mathbf{K}_i, \quad (23)$$

which when inserted into the definition of Fisher information gives

$$\mathbf{F}_{L_i} = E_{\mathbf{y}_i|\boldsymbol{\theta}^{(a)}} \left[\mathbf{K}_i \mathbf{K}_i^T \right] = \mathbf{H}_i^T \mathbf{C}_{\mathbf{y}_i}^{-1} \mathbf{H}_i \quad (24)$$

as the Fisher information for a single link in the network. Since we have assumed that the random variables $\{b_i, \epsilon_i\}$ are independent across links, the data $\{\mathbf{y}_i\}$ represent independent observations of $\boldsymbol{\theta}^{(a)}$. The additivity property of Fisher information for independent observations gives

$$\mathbf{F}_L = \sum_{i=1}^{N} \mathbf{F}_{L_i} = \sum_{i=1}^{N} \mathbf{H}_i^T \mathbf{C}_{\mathbf{y}_i}^{-1} \mathbf{H}_i$$

$$= \sum_{i=1}^{N} \mathbf{H}_i^T \left(\sigma_b^2 \mathbf{1}_n \mathbf{1}_n^T + \sigma_\epsilon^2 \mathbf{I}_n \right)^{-1} \mathbf{H}_i \quad (25)$$

as the expression for the Fisher information matrix of data collected from our uncalibrated network across all links. If the network were "perfectly calibrated" such that all bias parameters were known and removed, (25) reduces to

$$\mathbf{F}_{LC} = \frac{1}{\sigma_\epsilon^2} \mathbf{X}^T \mathbf{X}, \tag{26}$$

where $\mathbf{X}$ indicates the stacked matrices $\mathbf{X}_i$, and the subscript C indicates a calibrated or bias free network. This is the same matrix derived in [10] for their imaging problem, in which the stationary system took baseline readings in empty space before adding the objects under test.

For the prior distribution on the image and path loss parameters, we will assume that $\boldsymbol{\theta}^{(\alpha)}$ is also Gaussian distributed with mean $\boldsymbol{\mu}_{\boldsymbol{\theta}^{(\alpha)}}$ and covariance $\mathbf{C}_{\boldsymbol{\theta}^{(\alpha)}}$. The covariance structure is defined by (8), with α assumed uncorrelated with the image pixels. By very similar derivation it can be shown that

$$\mathbf{F}_P = \mathbf{C}_{\boldsymbol{\theta}^{(\alpha)}}^{-1}, \tag{27}$$

which defines all necessary parameters to compute the bound in (17). Note that while (17) gives a variance bound for *each* pixel, we will generally average over all pixels to compute an average bound for the entire image.

VI. PERFORMANCE SIMULATIONS

In this section we analyze the performance of our proposed convex EN solution approach with respect to the theoretical bounds derived in Section V. We attempt to choose parameter values which are realistic and also representative of the conditions seen in our experimental results of Section VII. In our simulations, we assume a 32×32 pixel image representing a $4.8\text{m} \times 4.8\text{m}$ area. The network of UWB nodes is mobile and each node moves independently through a larger 16×16 m area encompassing the image in a random-trajectory fashion. Our network is assumed to have a bias standard deviation $\sigma_b = 3$ dB and measurement noise standard deviation $\sigma_\epsilon = 3$ dB. Test images are generated according to a Gaussian distribution with a mean SLF value of 3 dB/m and pixel covariance defined by (8). We choose this prior image distribution for a fair comparison with standard Tikhonov regularization, which would be optimal for the Gaussian case *if* the network were perfectly calibrated. The simulated path loss exponent α is also Gaussian with mean 1 and standard deviation 0.1.

We measure the root-mean-squared error (RMSE) performance of both our proposed solution in (15), and our proposed solution ignoring the random effects and path loss, $\{b_i, \alpha\}$, and instead using only their mean values. These are assumed to be known from a measurement experiment such as that given in Fig. 2. For comparison, we also simulate the performance of the standard Tikhonov regularization used in e.g. [10], also ignoring random effects. The Bayesian CRLBs are also computed, where we use both our mixed effects Fisher information from (25) and the "calibrated" Fisher information in (26) as separate cases. Results are displayed in Fig. 4. In the first simulation we examine the average RMSE as a function of node count, assuming each node takes $n = 30$ measurements as it moves through the area. The results are shown in the top plot of Fig. 4. We note the superior performance of our
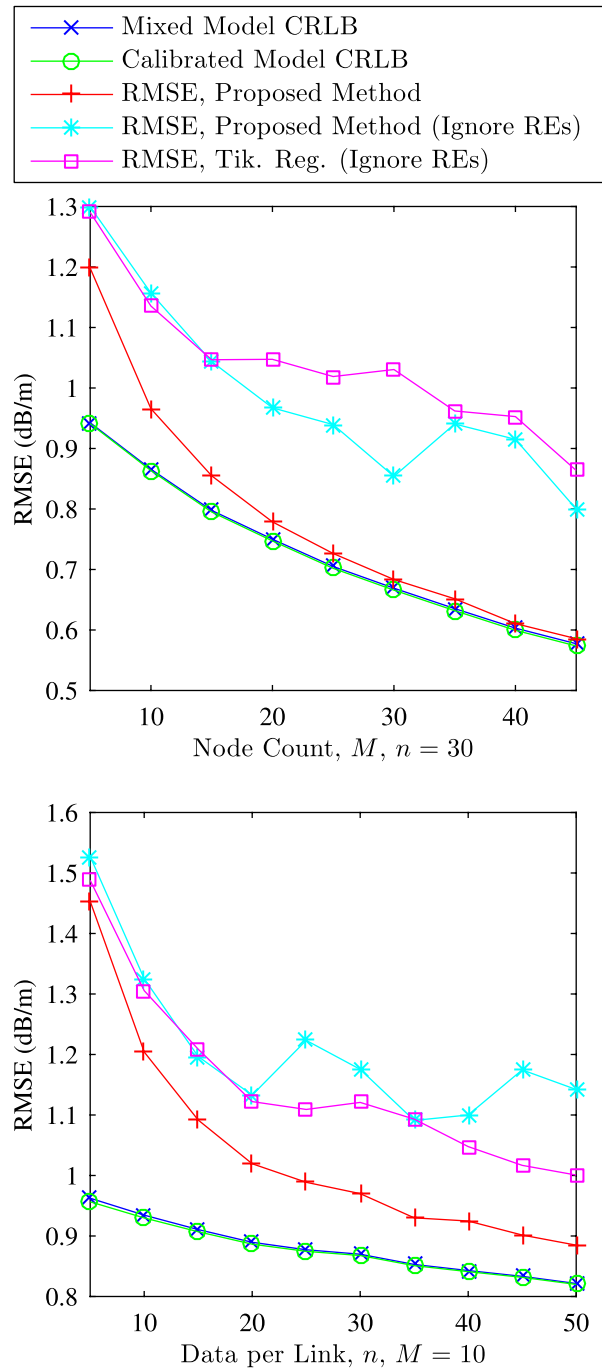

Fig. 4. Comprehensive performance simulation results, varying node count M (top) and data per link n (bottom). 25 images were simulated and estimated per data point.

method when random effects are considered and estimated across all values of M with respect to the Bayesian CRLBs. In fact our method virtually achieves the lower bound for large M. Also of interest is that the mixed model lower bound is only trivially larger than the calibrated model lower bound. These results suggest that the influence of the random effects and path loss $\{b_i, \alpha\}$ can be mitigated, since the bound is taken with respect to estimating fixed unknown parameter $\boldsymbol{\theta}^{(\alpha)}$. The difference between the two bounds would increase, however, if the bias variance σ_b^2 increased with respect to the noise variance σ_ϵ^2.

TABLE I
TOMOGRAPHIC MAPPING CAMPAIGN SUMMARY

	Exp. I	Exp. II	Exp. III
Number of discrete nodes		8	
Number of radio links, N		224	
Localization error RMSE		< 2.0 cm	
UWB pulse bandwidth		$3.3 - 5.5$ GHz	
UWB pulse duration		~ 4 ns	
UWB pulses per measurement		128	
Approx. avg. pulse power		-14.78 dBm	
Pixel size	0.1 m	0.15 m	0.15 m
Image dimensions	30×60	47×60	37×37
Data size, N_T	8512	10304	9856
Data per link, n	38	46	44
Reg. parameter λ_1	0.1350	0.1068	0.0936
Reg. parameter λ_2	1.000	0.9770	0.6000
Est. object(s) attenuation	8.1 dB	4.15, 7.64 dB	3.72 dB
Measured object(s) attenuation	14.5 dB	14.5, 14.5 dB	6.3 dB
Est. α	1.063	0.992	1.284
SSIM index	0.891	0.802	0.448
Pixel occupancy index	0.978	0.977	0.876

For our second simulation we assume a network of $M = 10$ nodes and instead vary the data collected for each link i. The results are shown in the bottom plot of Fig. 4. We again observe improving performance as more data becomes available to each link in the network. The lower bound on performance does not decrease as rapidly, though the total data size N_T is growing only linearly with n in this case. In both simulations, we see a clear performance degradation when the random effects are ignored. In fact, since Tikhonov Regularization can be shown to be an MMSE estimator for Gaussian distributed data with Gaussian prior, other methods of reconstruction are not likely to improve upon the indicated results without considering the random effects.

VII. EXPERIMENTAL RESULTS

In this section we validate our forward model and image reconstruction techniques using real experimental data from a variety of test setups containing attenuating objects. The experiments were performed using our Cognitive Spectrum Operations Testbed (CSOT). Originally introduced as RadioBOT in [47], CSOT is designed for performing spatially-oriented cognitive radio research in mobile networks. The system consists of eight mobile radio nodes, each with its own host computer, motorized base, radio hardware, and 4ft antenna mast. A primary difficulty in RTI research has been collection of quality real data. These tomographic experiments have resulted in collection of high fidelity data sets to address this issue.

The installed hardware of interest in this work is the aforementioned P410 UWB radio from Time Domain. The radio transmits and samples UWB pulses as described in Section II-A for each pairwise link in the network. Note that each CSOT node has 2 duplex UWB antenna ports, and both are used. This results in a system with 224 useful links from only 8 mobile nodes. The transmitted power and bandwidth are compliant with FCC regulations for a UWB system for general use. Received signal scans are converted to DPSS measurements as in Section II-B, and the esimated SLF is computed via the methods of Section IV. Common and individual experimental parameters are summarized in Table I.

To establish the correct pixel weighting described in Section III, accurate position information must be available to the nodes at each time step. All position data for our experiments are also provided by the UWB radios by our cooperative localization algorithms described in [29] and [30] Our localization algorithm uses precision ranging between nodes via time-of-flight measurements, another common application of UWB systems. The localization error is < 2 cm in LOS conditions. Thus, the same measured waveforms and hardware are used for both localization and tomographic mapping. We emphasize this natural SLAM characterization; a mobile network already utilizing UWB hardware for localization purposes could also perform our tomographic mapping in parallel. The UWB's low power and wide bandwidth make harmful interference very unlikely, enabling compatibility with other RF communications hardware.

We also note that it is difficult to accurately establish the true SLF in an experimental setting, and thus to compute the RMSE of the estimated images. Still, it is beneficial to quantify the estimated SLF image quality in some sense. We compute two different metrics for this purpose. First is the well known structural similarity (SSIM) metric [48], which compares a processed or degraded image to a reference. The SSIM attempts to measure how well structure is preserved, an important property of subjectively high quality images. Higher values of SSIM are better, with the maximum value of 1 occurring only when both images are identical. The reference images we use here are binary, equal to one where a pixel is occupied by an attenuating object, and zero elsewhere. To compare with the reference, the estimated SLF images are scaled to the range [0, 1], ignoring the negative sign.

For the second metric, we use the same reference image and scaled SLF to compute a simple pixel occupancy index. This is intended to measure how spatially accurate the image reconstruction is at detecting the objects in the experiments. The scaled SLF is threshold-ed to create a binary estimate; pixels less than 0.25 are treated as zero, and pixels greater than 0.25 are set to one. The pixel occupancy index is then defined to be the percentage of total pixels where the reference image and binary SLF estimate are equal. Thus, the index falls in the range [0, 1]; higher values being better. Both the SSIM and pixel occupancy indices are provided in Table I. The following subsections detail the particulars of the three experiments performed.

A. Experiment I: Hallway, Single Object

Our first experiment was performed in a laboratory building hallway, with the image encompassing an area approximately 3×6 m in size. The confined space, with large metal doors and close walls is intended to create a multipath rich environment for the system to overcome. A single 1.22 m wall section in the center is the target to be imaged; broadband RF absorbing foam was used to create opacity to the UWB signals. The test utilized 3 stationary and 5 mobile nodes. The experiment setup, binary reference image, and reconstructed images are displayed in Fig. 5. We note that the position of the wall is well-contrasted with the free space background, which is
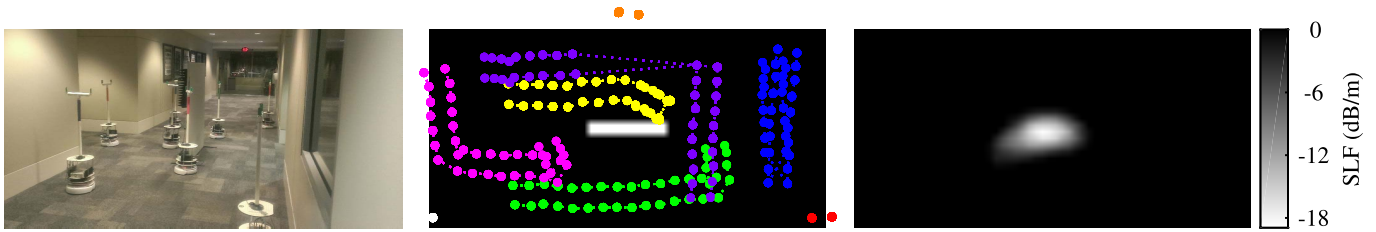
Fig. 5. Experiment I setup and results. Left: Hallway test setup, showing the attenuating object and CSOT nodes. Middle: overhead schematic view/binary reference image of the test area. Data sampling locations for each node are indicated by colored dots. Right: SLF image reconstruction from DPSS measurements.
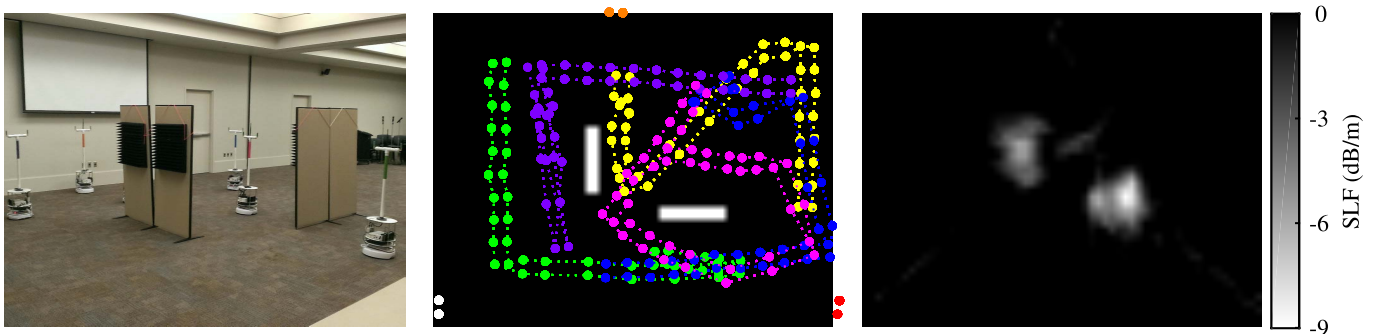

Fig. 6. Experiment II setup and results. Left: Conference room test setup, showing the attenuating objects and CSOT nodes. Middle: overhead schematic view/binary reference image of the test area, with colored dots showing data sampling locations. Right: SLF image reconstruction from DPSS measurements.

correctly estimated to have an attenuation of 0 dB. As a result, the SSIM and pixel occupancy index given in Table I are the highest of the campaign.

To estimate the attenuation of the wall from the SLF image, we take a straight line, perpendicular path through the wall at its brightest point. Doing so gives an estimated total attenuation of 8.1 dB, an approximation of the laboratory measured attenuation of 14.5 dB. Note that in general, shadowing loss values obtained from the tomographic image will tend to underestimate the true value, since the regularization applied tends to bias the solution toward zero.

B. Experiment II: Large Room, Two Objects

Our second experiment seeks to differentiate and estimate the attenuation of two 1.22 m objects separated by a gap of 1.58 m. The experiment was performed in a large conference room with a larger test area of 7×9 m. The same type of attenuating foam was used for the walls, and the test again used 3 stationary and 5 mobile nodes. The results are shown in Fig. 6. The objects are well differentiated, though we do note some over-smoothing with our systematic regularization parameter search. This lowers the SSIM vs. Experiment I, though the occupancy index is still quite high. In this case, the wall sections have an estimated attenuation of 4.15 dB (left) and 7.64 dB (right) using the same perpendicular paths as Experiment I.

C. Experiment III: Through-Wall Imaging

The final experiment seeks to demonstrate our proposed techniques for a through-wall image, an application of RTI which has been frequently proposed in the literature. That is, we wish to estimate not only the location and attenuation of visible features, but also those which might be obstructed behind walls. To do this, a 2.44×2.44 m artificial building was constructed from standard drywall material, shown in Fig. 7. Since the drywall is highly transparent to the UWB signal, very thin RF absorbing foam was added to the inside surface to simulate a much thicker material. Another wall section was placed in the center, and data was collected as shown by surveying around the perimeter using 4 mobile and 4 stationary nodes. As shown, the image reconstruction is able to resolve the empty space inside the structure and partially separate the interior object. Estimates of the outer wall attenuation average 3.72 dB, measured diagonally through each corner. Laboratory measurements of the outer wall attenuation yielded 6.3 dB. The greater difficulty in reconstructing this image is also evident in the lower SSIM and occupancy indices, which is consistent with the subjectively lower image quality.

The through-wall imaging performance could be improved in several ways. One could depart from our systematic approach to finding $\{\lambda_1, \lambda_2\}$ and manually tune these parameters, as well as place additional constraints on bias vector **b** and path loss α. As suggested in Section IV-B and [39], the wall sections could be better estimated by altering the spatial shape of the prior image covariance. We leave this increased scope as a topic for future research.

D. Penalty for Ignoring Random Effects

The simulation results from Section VI suggest that ignoring link bias and path loss parameters (i.e., using assumed or empirical values) carries a performance penalty regardless of the method used to estimate the image. To get a sense of the influence these parameters may have in
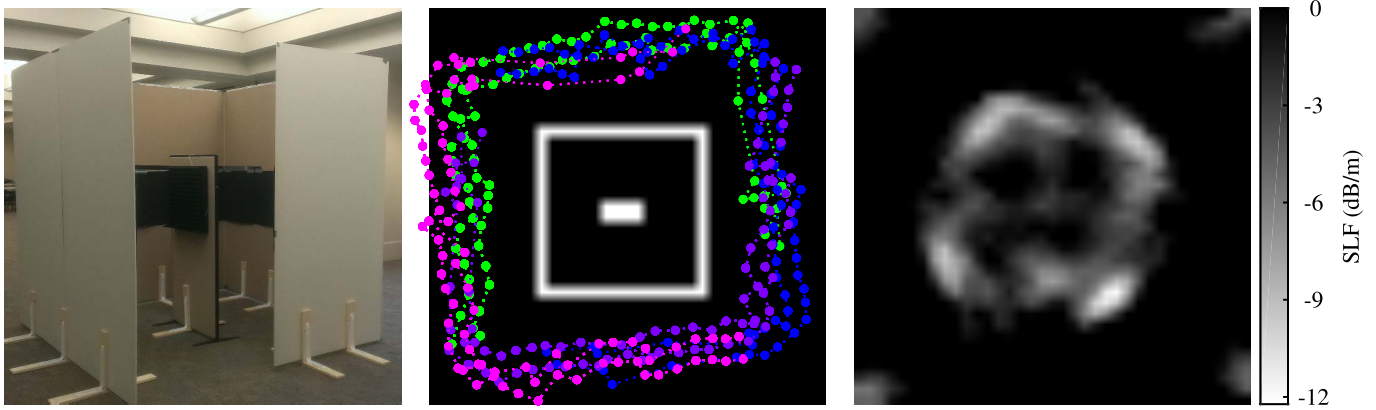
Fig. 7. Experiment III setup and results. Left: Artificial building test setup, with cutaway showing the interior object. Middle: overhead schematic view/binary reference image of the test area, with colored dots showing data sampling locations. Right: SLF image reconstruction from DPSS measurements.
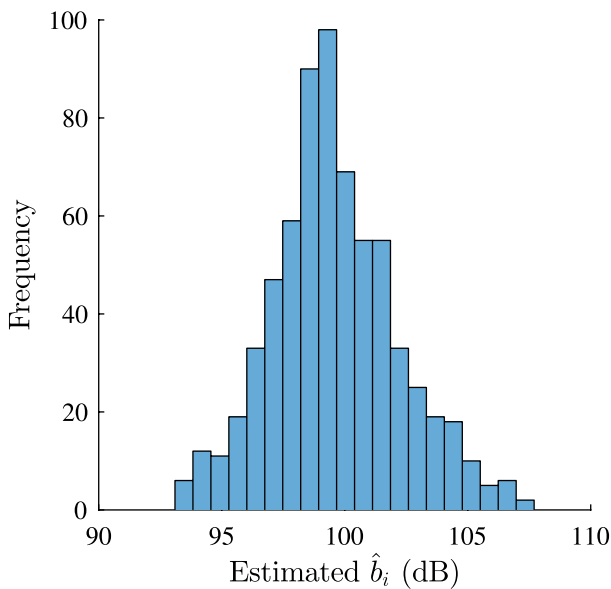

Fig. 8. Histogram plot showing distribution of values of the estimated $\{\hat{b}_i\}$ across all experiments. The sample mean $\hat{\mu}_b = 99.60$ dB and sample standard deviation $\hat{\sigma}_b = 2.59$ dB.

Fig. 9. Tikhonov regularization solution for Experiment II when ignoring the random effects. $\hat{b}_i = \hat{b} = 104.1$ dB, $\hat{\alpha} = 0.941$ from Fig. 2. The L-curve method was used to determine $\lambda_2 = 1.003$, and constraint $\hat{\theta} \leq 0$ is applied.

practice, we plot the histogram of the estimated $\{\hat{b}_i\}$ in Fig. 8. The empirical distribution of values gives confidence to our original assumption that this parameter carries a Gaussian distribution; in this case the sample mean is $\hat{\mu}_b = 99.60$ dB and sample standard deviation is $\hat{\sigma}_b = 2.59$ dB.

To visualize the effect of ignoring these parameters, we estimate the standard Tikhonov regularization solution on the data for Experiment II, assuming that all links carry the same bias $\hat{b}_i = \hat{b} = 104.1$ dB and path loss exponent $\alpha = 0.941$ obtained empirically from Fig. 2. The result is shown in Fig. 9. The degradation in performance is evident in comparison with our method, particularly the streaking between positions of the stationary nodes. This example illustrates the important observation made in Section II-C that results for a single pair of nodes may not generalize well to an entire network, despite the estimated parameters strongly fitting the data. This is true even if all nodes share the same hardware, antennas, and power levels, as in our experiments.

VIII. CONCLUSION

In this work we have presented a novel mixed-effects modeling technique for aggregating UWB signal strength measurements in an uncalibrated, mobile network, for the purposes of performing static radio tomographic imaging. We have proposed to use the DPSS metric from a UWB signal as a practical means of managing multipath propagation, in contrast with other approaches. UWB has gained popularity for use in GPS-denied indoor environments, and our imaging may be performed in parallel with cooperative localization of the network. This is very attractive for distributed sensor networks already using UWB for localization or communication, since the network may immediately expand to performing SLAM during localization.

To estimate the unknown SLF image, we have proposed to use a modified convex form of EN regularization. Our simulation results show very attractive performance relative to the derived Bayesian CRLB in the presence of the random effects. In our experimental results we have shown the performance of our methods to estimate both the positions as well as the spatial loss field present in the environment using a mobile, cooperative network.[3]

---

[3]Datasets are available to other researchers for testing new algorithms via GitHub: https://github.com/bbeck6/CSOT-UWB-Tomography-Data.git.

Future research could focus on a key observation that the UWB pulse signal also captures significant channel information. While the DPSS rejects all energy not propagating along the line of sight, this energy still carries information about the reflective environment. This channel information could be used to also characterize the reflective environment, as in a multistatic radar. The tomographic image (transmitted signals) and radar image (reflected signals) could be highly complementary in characterizing the RF environment.

Our mixed model framework for characterizing biased network parameters could also be applied to other signal processing problems where data is collected from multiple low-cost, uncalibrated sensors. As wireless sensor networks continue to proliferate in greater numbers, directly estimating such parameters from the data becomes more attractive. Results could be applied wherever absolute signal levels are crucial, or when measurements must be compared among uncalibrated sensors.

REFERENCES

[1] H. Durrant-Whyte and T. Bailey, "Simultaneous localization and mapping: Part I," *IEEE Robot. Autom. Mag.*, vol. 13, no. 2, pp. 99–110, Jun. 2006.

[2] T. Bailey and H. Durrant-Whyte, "Simultaneous localization and mapping (SLAM): Part II," *IEEE Robot. Autom. Mag.*, vol. 13, no. 3, pp. 108–117, Sep. 2006.

[3] R. C. Luo and C. C. Lai, "Multisensor fusion-based concurrent environment mapping and moving object detection for intelligent service robotics," *IEEE Trans. Ind. Electron.*, vol. 61, no. 8, pp. 4043–4051, Aug. 2014.

[4] E. Dall'Anese, S.-J. Kim, and G. B. Giannakis, "Channel gain map tracking via distributed Kriging," *IEEE Trans. Veh. Technol.*, vol. 60, no. 3, pp. 1205–1211, Mar. 2011.

[5] E. J. Baranoski, "Through-wall imaging: Historical perspective and future directions," *J. Franklin Inst.*, vol. 345, no. 6, pp. 556–569, 2008.

[6] D. A. Hill, "Radio propagation in a coal seam and the inverse problem," *J. Res. Nat. Bureau Standards*, vol. 89, no. 5, p. 36, Sep./Oct. 1984.

[7] L. Stolarczyk, G. Rogers, and P. Hatherly, "Comparison of radio imaging method (RIM) electromagnetic wave tomography with in-mine geological mapping in the Liddell, Bulli and Wongawilli coal seams," *Exploration Geophys.*, vol. 19, nos. 1–2, pp. 169–170, Jan. 1988.

[8] N. Pendock, "Radio-wave tomography for geological mapping," *Proc. SPIE*, vol. 1942, pp. 96–104, Nov. 1993.

[9] L. Lo Monte, D. Erricolo, F. Soldovieri, and M. C. Wicks, "Radio frequency tomography for tunnel detection," *IEEE Trans. Geosci. Remote Sens.*, vol. 48, no. 3, pp. 1128–1137, Mar. 2010.

[10] J. Wilson and N. Patwari, "Radio tomographic imaging with wireless networks," *IEEE Trans. Mobile Comput.*, vol. 9, no. 5, pp. 621–632, May 2010.

[11] N. Patwari and J. Wilson, "RF sensor networks for device-free localization: Measurements, models, and algorithms," *Proc. IEEE*, vol. 98, no. 11, pp. 1961–1973, Nov. 2010.

[12] J. Wilson and N. Patwari, "See-through walls: Motion tracking using variance-based radio tomography networks," *IEEE Trans. Mobile Comput.*, vol. 10, no. 5, pp. 612–621, May 2011.

[13] J. Wilson, N. Patwari, and F. G. Vasquez, "Regularization methods for radio tomographic imaging," in *Proc. Virginia Tech Symp. Wireless Pers. Commun.*, 2009, pp. 1–9.

[14] N. Patwari and P. Agrawal, "NeSh: A joint shadowing model for links in a multi-hop network," in *Proc. IEEE Int. Conf. Acoust., Speech, Signal Process. (ICASSP)*, Mar./Apr. 2008, pp. 2873–2876.

[15] B. R. Hamilton, X. Ma, and R. J. Baxley, "SAL: Shadowing assisted localization," in *Proc. IEEE Statist. Signal Process. Workshop (SSP)*, Jun. 2011, pp. 229–232.

[16] Y. Mostofi, "Cooperative wireless-based obstacle/object mapping and see-through capabilities in robotic networks," *IEEE Trans. Mobile Comput.*, vol. 12, no. 5, pp. 817–829, May 2013.

[17] A. Gonzalez-Ruiz and Y. Mostofi, "Cooperative robotic structure mapping using wireless measurements—A comparison of random and coordinated sampling patterns," *IEEE Sensors J.*, vol. 13, no. 7, pp. 2571–2580, Jul. 2013.

[18] A. Gonzalez-Ruiz, A. Ghaffarkhah, and Y. Mostofi, "An integrated framework for obstacle mapping with see-through capabilities using laser and wireless channel measurements," *IEEE Sensors J.*, vol. 14, no. 1, pp. 25–38, Jan. 2014.

[19] R. J. Fontana, "Recent system applications of short-pulse ultra-wideband (UWB) technology," *IEEE Trans. Microw. Theory Techn.*, vol. 52, no. 9, pp. 2087–2104, Sep. 2004.

[20] F. J. Yanovsky, V. E. Ivashchuk, and V. P. Prokhorenko, "Through-the-wall surveillance technologies," in *Proc. 6th Int. Conf. Ultra-wideband Ultrashort Impulse Signals (UWBUSIS)*, Sep. 2012, pp. 30–33.

[21] C. R. P. Dionisio, S. Tavares, M. Perotoni, and S. Kofuji, "Experiments on through-wall imaging using ultra wideband radar," *Microw. Opt. Technol. Lett.*, vol. 54, no. 2, pp. 339–344, 2012.

[22] S. Nag, M. A. Barnes, T. Payment, and G. Holladay, "Ultrawideband through-wall radar for detecting the motion of people in real time," *Proc. SPIE*, vol. 4744, pp. 48–57, Jul. 2002.

[23] Q. Huang, L. Qu, B. Wu, and G. Fang, "UWB through-wall imaging based on compressive sensing," *IEEE Trans. Geosci. Remote Sens.*, vol. 48, no. 3, pp. 1408–1415, Mar. 2010.

[24] S. Bartoletti, A. Conti, A. Giorgetti, and M. Z. Win, "Sensor radar networks for indoor tracking," *IEEE Wireless Commun. Lett.*, vol. 3, no. 2, pp. 157–160, Apr. 2014.

[25] S. Bartoletti, A. Giorgetti, M. Z. Win, and A. Conti, "Blind selection of representative observations for sensor radar networks," *IEEE Trans. Veh. Technol.*, vol. 64, no. 4, pp. 1388–1400, Apr. 2015.

[26] V. Casadei, N. Nanna, and D. Dardari, "Experimental study in breath detection and human target ranging in the presence of obstacles using ultra-wideband signals," *Int. J. Ultra Wideband Commun. Syst.*, vol. 2, no. 2, pp. 116–123, 2011.

[27] S. Gezici *et al.*, "Localization via ultra-wideband radios: A look at positioning aspects for future sensor networks," *IEEE Signal Process. Mag.*, vol. 22, no. 4, pp. 70–84, Jul. 2005.

[28] N. Patwari, J. N. Ash, S. Kyperountas, A. O. Hero, R. L. Moses, and N. S. Correal, "Locating the nodes: Cooperative localization in wireless sensor networks," *IEEE Signal Process. Mag.*, vol. 22, no. 4, pp. 54–69, Jul. 2005.

[29] B. Beck and R. Baxley, "Anchor free node tracking using ranges, odometry, and multidimensional scaling," in *Proc. IEEE Int. Conf. Acoust., Speech Signal Process. (ICASSP)*, May 2014, pp. 2209–2213.

[30] B. Beck, R. Baxley, and J. Kim, "Real-time, anchor-free node tracking using ultrawideband range and odometry data," in *Proc. IEEE Int. Conf. Ultra-wideband (ICUWB)*, Sep. 2014, pp. 286–291.

[31] A. Gonzalez-Ruiz, A. Ghaffarkhah, and Y. Mostofi, "A comprehensive overview and characterization of wireless channels for networked robotic and control systems," *J. Robot.*, vol. 2011, Oct. 2011, Art. no. 340372.

[32] A. Edelstein and M. Rabbat, "Background subtraction for online calibration of baseline RSS in RF sensing networks," *IEEE Trans. Mobile Comput.*, vol. 12, no. 12, pp. 2386–2398, Dec. 2013.

[33] D. Maas, J. Wilson, and N. Patwari, "Toward a rapidly deployable radio tomographic imaging system for tactical operations," in *Proc. 38th IEEE Conf. Local Comput. Netw. (LCN)*, Oct. 2013, pp. 203–210.

[34] B. R. Hamilton, X. Ma, R. J. Baxley, and S. M. Matechik, "Propagation modeling for radio frequency tomography in wireless networks," *IEEE J. Sel. Topics Signal Process.*, vol. 8, no. 1, pp. 55–65, Feb. 2014.

[35] B. Dewberry and W. Beeler, "Increased ranging capacity using ultrawideband direct-path pulse signal strength with dynamic recalibration," in *Proc. IEEE/ION Position Location Navigat. Symp. (PLANS)*, Apr. 2012, pp. 1013–1017.

[36] A. F. Molisch, "Ultrawideband propagation channels-theory, measurement, and modeling," *IEEE Trans. Veh. Technol.*, vol. 54, no. 5, pp. 1528–1545, Sep. 2005.

[37] D. Cassioli, M. Z. Win, and A. F. Molisch, "The ultra-wide bandwidth indoor channel: From statistical model to simulations," *IEEE J. Sel. Areas Commun.*, vol. 20, no. 6, pp. 1247–1257, Aug. 2002.

[38] P. Agrawal and N. Patwari, "Correlated link shadow fading in multi-hop wireless networks," *IEEE Trans. Wireless Commun.*, vol. 8, no. 8, pp. 4024–4036, Aug. 2009.

[39] B. Beck, R. Baxley, and X. Ma, "Regularization techniques for floor plan estimation in radio tomographic imaging," in *Proc. IEEE Global Conf. Signal Inf. Process. (GlobalSIP)*, Dec. 2013, pp. 177–180.

[40] E. Demidenko, *Mixed Models: Theory and Applications With R* (Wiley Series in Probability and Statistics), 2nd ed. Hoboken, NJ, USA: Wiley, 2013.

[41] N. M. Laird and J. H. Ware, "Random-effects models for longitudinal data," *Biometrics*, vol. 38, no. 4, pp. 963–974, 1982.

[42] R. C. Aster, B. Borchers, and C. H. Thurber, *Parameter Estimation and Inverse Problems*, 2nd ed. San Diego, CA, USA: Academic, 2012.

[43] H. Zou and T. Hastie, "Regularization and variable selection via the elastic net," *J. Roy. Stat. Soc.*, vol. 67, no. 2, pp. 301–320, 2005.

[44] A. M. Stuart, "Inverse problems: A Bayesian perspective," *Acta Numer.*, vol. 19, pp. 451–559, Apr. 2010.

[45] M. C. Grant and S. P. Boyd, "Graph implementations for nonsmooth convex programs," in *Recent Advances in Learning and Control Lecture Notes in Control and Information Sciences*, V. D. Blondel, S. P. Boyd, and H. Kimura, Eds. London, U.K.: Springer London, 2008, pp. 95–110.

[46] R. D. Gill and B. Y. Levit, "Applications of the van Trees inequality: A Bayesian Cramér-Rao bound," *Bernoulli*, vol. 1, nos. 1–2, pp. 59–79, 1995.

[47] B. M. Beck, J. H. Kim, R. J. Baxley, and B. T. Walkenhorst, "RadioBOT: A spatial cognitive radio testbed," in *Proc. IEEE Aerosp. Conf.*, Mar. 2013, pp. 1–9.

[48] Z. Wang, A. C. Bovik, H. R. Sheikh, and E. P. Simoncelli, "Image quality assessment: From error visibility to structural similarity," *IEEE Trans. Image Process.*, vol. 13, no. 4, pp. 600–612, Apr. 2004.

Xiaoli Ma (F'15) received the B.S. degree in automatic control from Tsinghua University, Beijing, China, in 1998, the M.S. degree in electrical engineering from the University of Virginia in 2000, and the Ph.D. degree in electrical engineering from the University of Minnesota in 2003. She joined the Department of Electrical and Computer Engineering, Auburn University, where she served as an Assistant Professor until 2005. Since 2006, she has been with the School of Electrical and Computer Engineering, Georgia Institute of Technology, where she is currently a Professor.

Her research focuses on networking and communications, including network performance analysis, transceiver designs for wireless time- and frequency-selective channels, channel estimation and equalization algorithms, carrier frequency synchronization for OFDM systems, performance analysis, and cooperative designs for wireless networks. She has been serving as a Senior Area Editor of the IEEE SIGNAL PROCESSING LETTERS since 2014 and *Elsevier Digital Signal Processing* since 2012, and was an Associate Editor of the IEEE SIGNAL PROCESSING LETTERS from 2007 to 2009 and the IEEE TRANSACTIONS ON WIRELESS COMMUNICATIONS from 2008 to 2013. She received the Lockheed Martin Aeronautics Company Dean's Award for Teaching Excellence by the College of Engineering in 2009, and Outstanding Junior Faculty Award by the School of Electrical and Computer Engineering in 2010 at Georgia Tech.

Brian Beck (S'05) received the B.S. degree in electrical engineering and the M.B.A. degree from Ohio State University, Columbus, OH, USA, in 2007 and 2009, respectively. He is currently pursuing the Ph.D. degree in electrical and computer engineering with the Georgia Institute of Technology, Atlanta, GA, USA. He has been a Research Engineer with the Information and Communications Laboratory, Georgia Tech Research Institute, since 2014.

His current research interests include radio tomographic imaging, sensor localization and tracking, sensor registration, and inverse problems.

Robert Baxley (SM'14) received the B.S., M.S., and Ph.D. degrees from the Georgia Institute of Technology, all in electrical engineering. From 2008 to 2014, he was with the Georgia Tech Research Institute (GTRI), where he served as the Director of the Software Defined Radio Laboratory. While at GTRI, he led the GTRI team that placed second out of 90 teams in the DARPA Spectrum Challenge. He is currently the Chief Engineer with Bastille Networks. He is an Adjunct Faculty Member with the Georgia Tech School of Electrical and Computer Engineering.

His current research interests are in the areas of cognitive radio, wireless security, and signal processing for communications systems. From 2012 to 2014, he served as an Associate Editor of *Digital Signal Processing*. He is a member of the Association of Old Crows. In the course of his graduate work, he was a recipient of the Sigma Xi Award, the National Science Foundation Graduate Research Fellowship Program Award, the Grand Prize in the SAIC Student Paper Competition, and the Georgia Tech Center for Signal Image Processing Outstanding Research Award.